PHYSICAL REVIEW B **90**, 155402 (2014)

Relaxation dynamics of carbon nanotubes of enriched chiralities

Olga A. Dyatlova,[1] Christopher Koehler,[2] Peter Vogel,[1] Ermin Malic,[2] Rishabh M. Jain,[3] Kevin C. Tvrdy,[3] Michael S. Strano,[3] Andreas Knorr,[2] and Ulrike Woggon[1]

[1]*Institut für Optik und Atomare Physik, Technische Universität Berlin, 10623 Berlin, Germany*
[2]*Institut für Theoretische Physik, Technische Universität Berlin, 10623 Berlin, Germany*
[3]*Department of Chemical Engineering, MIT, 66-566 Cambridge, Massachusetts 02139, USA*

(Received 13 August 2014; revised manuscript received 29 August 2014; published 1 October 2014)

In our work we combined experimental and theoretical investigations of the relaxation dynamics of the single wall carbon nanotubes (SW-CNTs) in solution samples with enriched chiralities of (7,5) and (7,6) species. In two-color pump-probe studies we observe three-exponential decay in the differential transmission spectra in the range of few picoseconds, tens of picoseconds, and hundreds of picoseconds. Decay curves are very similar for both SW-CNT chiralities under resonant excitation and probing of excited and ground state transition energies, respectively. Both types of tubes exhibit no changes in decay for the different excitation energies in the range ±50 meV around the excited state. By tuning the probe pulse towards energies higher then ground state (up to +350 meV) we observe acceleration of the first decay component from 5.8 ps down to 1.6 ps. Our experimental results are supported by time resolved microscopic calculations based on carbon nanotube Bloch equations proving the fast decay component behavior being dominated through scattering with acoustic phonons.

DOI: 10.1103/PhysRevB.90.155402 PACS number(s): 42.65.Sf, 78.47.D−, 78.67.Ch, 63.22.Gh

I. INTRODUCTION

Since the discovery of carbon nanotubes the substantial fundamental studies of their optical and electronic properties have been conducted, both experimentally and theoretically [1–3]. Carbon nanotubes also offer tremendous potential for the real life application devices development, such as microscopic nanotube conducting fibers [4], mechanical damping foam [5], mechanical and optical sensors [6], and other nanoscale optoelectronic devices [7,8]. A crucial point for the successful design of the last one is the thorough microscopic understanding of the ultrafast relaxation dynamics of nonequilibrium charge carriers of the tubes.

Many experiments on carrier relaxation dynamics in tubes have been conducted in a last decade exhibiting very different relaxation times which are rising from 40 fs [9,10] all the way up to microseconds [11], with steps at few hundred femtoseconds, few, tens and hundreds of picoseconds, as well as few nanoseconds. The explanation for these relaxation behavior is multiple. For example, the 40 fs time constant reported by Lanzani *et al.* [10] is assigned to decay of the second exciton into the first exciton. Exciton-exciton annihilation and low-energy phonons are discussed in Ref. [12], where the relaxation dynamics is reported at the time scale of a few hundred of femtoseconds, few, tens and hundreds of picoseconds. Decay times in ranges 0.3–1.2 ps and 5–20 ps reported by Ostojic *et al.* [13] are assigned to intraband and interband carrier recombination, respectively. Subpicosecond to picosecond components are often assigned to the relaxation in tube bundles [14,15]. The microsecond relaxation observed by Park *et al.* [11] is assigned to the triplet excited-state lifetime. In our previous work we observe the three exponential decay for four different species of single wall carbon nanotubes (SW-CNTs) in the solvent sample, and we show that the fast component of the relaxation dynamics τ_1 (in the range between 6 and 15 ps) is in a good agreement with theoretically predicted intraband scattering times with acoustic phonons [16].

One of the crucial difficulties for tubes studies is that the standard samples contain a diversity of SW-CNT species with different diameters and transition energies. Therefore even resonant excitation and probing of a selected tube species in pump-probe experiment is likely to cause the mixture of signals rising from different tube species with similar transition energies. Taking into account the diameter dependence of the theoretically predicted intraband scattering [16], as well as influence of the dielectric environment of the tubes onto relaxation dynamics [17,18], analysis and comparison of the experimental results can become nontrivial. One way around this problem is a single tube experiment, for example, individual metallic tubes have been studied by Gao *et al.* in Ref. [17] and exhibit hundreds of fs and ∼10 ps energy relaxation dynamics. The other way is to investigate chirality enriched samples with a high percentage of one tube species.

In this paper we combine top level "cooking" technique of the chirality-enriched SW-CNT sample preparation, theoretical calculations, and sophisticated two-color pump-probe measurements in order to investigate relaxation dynamics in SW-CNT. In our energy-selective two-color pump-probe measurements we study dependency of relaxation dynamics on excitation and probing energies and discover the acceleration of the fast (few picoseconds) decay component for higher probe energies. This acceleration we describe by theoretical findings. In addition we report no significant changes of the relaxation for different pump energies, which is also supported by theoretical calculations.

II. EXPERIMENT

Here we investigate two SW-CNT samples with chirality enriched (7,5) and (7,6) tubes, in the following referred to as "(7,5)-sample" and "(7,6)-sample," respectively. We prepare the SW-CNT following the same procedure we have published previously (see Refs. [19] and [20]) which is a gel based method demonstrated by Kataura and co-workers [21]. Briefly, 100 mg of HiPco SW-CNT in powder form is weighed and dispersed in 100 ml of 2 % wt aqueous sodium dodecyl sulfate (SDS) solution via sonication at 20 W for 20 hr using a 1/2″ tip

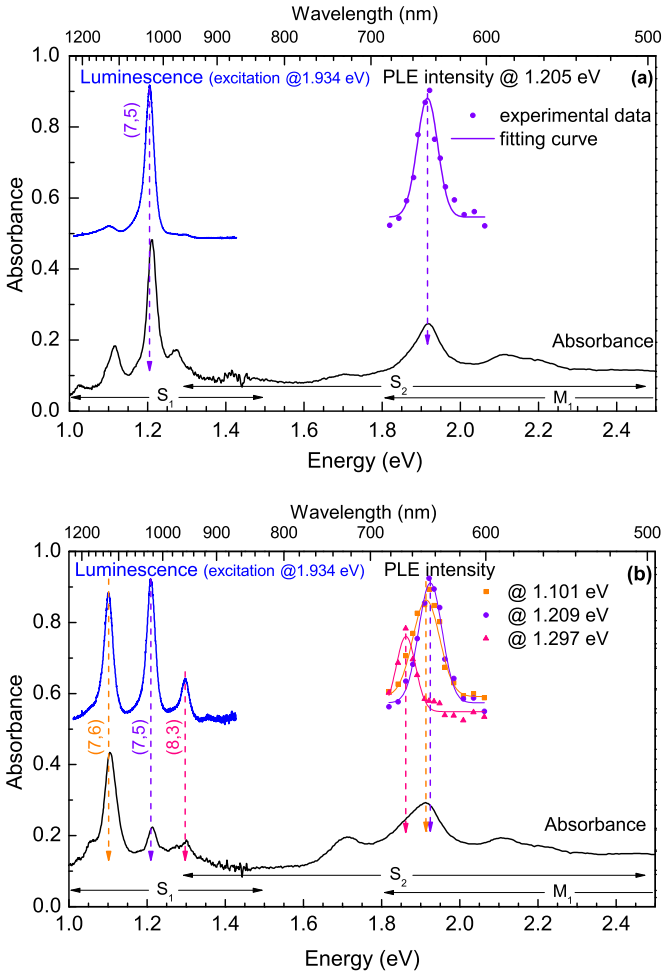

FIG. 1. (Color online) Absorption measurements (black curves) and photoluminescence intensity for the 1.934 eV excitation energy (blue curves) of the (7,5)- and (7,6)-samples, (a) and (b), respectively. In (a) with violet dots the intensity of the luminescence at the energy of 1.205 eV for 14 different excitation energies is shown; the solid line depicts the Gaussian fitting curve. Analogous in (b) with orange, violet, and pink dots the intensity of the luminescence at the energy of 1.101 eV, 1.209 eV, and 1.297 eV, respectively, are shown; the solid lines of according colors depict the fitting curves. Horizontal arrows indicate first and second exciton energy ranges of semiconducting tubes (S_1 and S_2) and first exciton range of metallic tubes (M_1).

sonicator. This sample is then ultracentrifuged at 187,000 × g for four hours. The 100 ml SW-CNT solution is passed through 14 ml of 2% wt SDS equilibrated Sephacryl at a rate of 3 ml/min. The flowed through SW-CNT solution that is passed through the column is collected in a separate container to iterate this procedure with. The column is then washed with 20 ml of 2% wt SDS solution and eluted with 20 ml of 5% wt SDS solution also at 3 ml/min. The process is then iterated over several columns.

Absorption and luminescence curves of (7,5)- and (7,6)-samples studied in the present paper are shown in Figs. 1(a) and 1(b), respectively. Absorption curves of both samples represent few pronounced peaks in the energy range which is associated with first exciton transition energy of the semiconducting tubes (denoted with S_1). For the (7,5)-sample [(7,6)-sample] the most pronounced absorption peak in S_1 region corresponds to the E_{11} transition energy of the (7,5) [(7,6)] tube. In the region of the second exciton transition energies of the semiconducting tubes (denoted with S_2) the most pronounced absorption peak of the (7,5)-sample corresponds to the E_{22} transition energy of (7,5) species, in spite of the (7,6)-sample, where the pronounced absorption corresponds to three species at once: (7,6), (7,5), and (8,3). Absorption measurements were performed using a Shimdzu UV-310PC spectrometer at a spectral resolution of 1 nm.

We estimate the chiral purity of the (7,5) [(7,6)] species for the (7,5)-sample [(7,6)-sample] to be 49% [24%], which means that at least the half (quarter) of the tubes presented in the (7,5)-sample [(7,6)-sample] are (7,5) [(7,6)] species. The chiral purity was estimated by integrating under the area of fitting the absorbance profiles to Lorentzian curves in the E_{11} region after subtracting a linear background as was done in Ref. [19].

The characterization of chirality enriched samples is done by the widely used photoluminescence excitation spectroscopy (PLE) method [22]. For the PLE experiment we use pulsed titanium sapphire laser (Ti:Sa) in combination with optical parametric oscillator (OPO); the excitation energies were tuned from 1.819 to 2.035 eV (that corresponds to the wavelength region from 609 to 682 nm) with step size between 11 and 26 meV (average step size 19 meV) in order to reach over all 14 different excitation energies. Examples of the luminescence curves for both samples are presented in Fig. 1. For more of a description of the experimental technique, see our earlier work [23].

In Fig. 2 experimentally measured PLE maps for the (7,5)- and (7,6)-samples are shown, labeled as (a) and (b), respectively. The points of high intensities are assigned to the (7,5) tube for the (7,5)-sample, and to (7,6), (7,5), and (8,3) tubes for the (7,6)-sample. The vertical intensity profiles of both PLE maps at the emission energy of the peaks are shown with dots in Fig. 1, along with Gaussian fitting curves. Thus we determine transition energies E_{11} and E_{22} for the tubes presented in both samples (energies are listed in Table I), which we further use to select pump and probe energies in two-color pump-probe measurements.

To perform energy-selective pump-probe experiments we use two synchronized laser systems as well as OPO, which allow us to tune pump and probe independently in a wide energy range and achieve desired wavelength combinations. In this paper we used two set-up configurations. Most of the measurements are done in the first configurations: The Ti:Sa laser serves as the master laser and is used to pump the OPO, which in its turn is used as a pump arm of the experiment (standard tunability range from 500 to 760 nm with a full width at half maximum (FWHM) of about 6 nm, pulse duration of about 150 fs, and repetition rate of 75.4 MHz). In this paper we used three excitation wavelengths (about 625, 645, and 660 nm), which correspond to 1.982, 1.923, and 1.880 eV with FWHM of 8 meV (the error bar of the central energy definition is about 2 meV). The pulse duration of the pump is determined to be 190 fs, by autocorrelation measurement. A fiber laser serves as the slave laser and is used for the probe arm (standard tunability range from 900 nm to 1.3 μm). We perform the control of the temporal pulse shape of the fiber

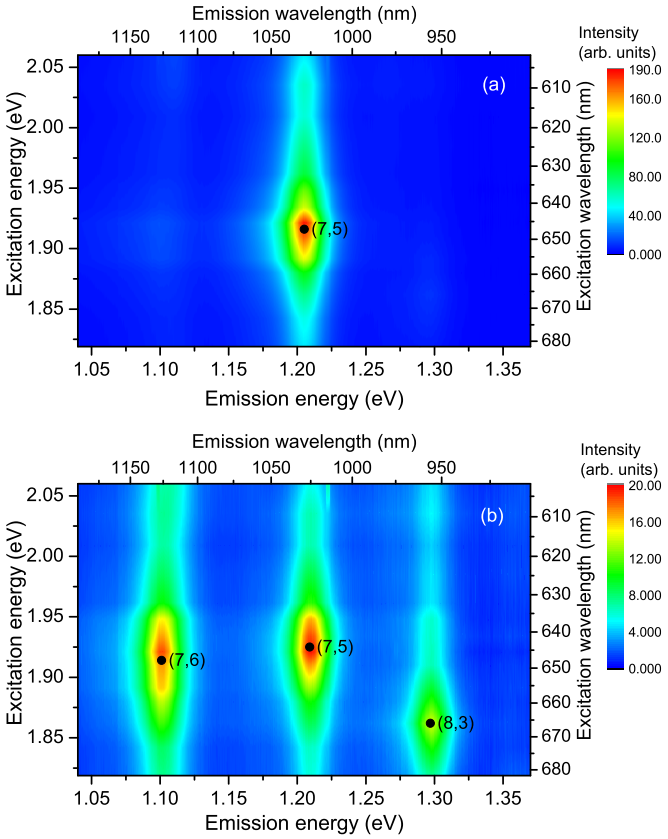

FIG. 2. (Color online) 3D contour plot of photoluminescence intensity versus excitation and emission energies for the SW-CNTs in (7,5)- and (7,6)-samples, (a) and (b), respectively.

laser by an external pulse shaper and detect it with commercial autocorrelator. In this paper we tuned the fiber laser mainly to tree probing wavelengths (about 1125, 1025, and 997 nm), which correspond to 1.102, 1.209, and 1.244 eV with FWHM of 8 to 10 meV (the error bar of the central energy definition is about 1 meV). The pulse duration of the fiber laser after the pulse shaper was kept below 300 fs. The used synchronization unit provides a time jitter in the range of 0.5 ps.

In a second configuration we use the OPO (in the same way) as a pump arm, but as a probe arm we take an output of the Ti:Sa laser. The OPO is based on periodically polled (PP) crystal which structure defines the pump wavelength of the OPO. We use two PP crystals with different poling periods and therefore reach two different probe wavelengths (about 793 and 837 nm) in the pump-probe experiment. Thus we tune the probe energies as high as 1.481 and 1.563 eV (±1 meV), with FWHM of 8 meV and pulse duration of about 200 fs.

TABLE I. List of the determined transition energies of the tubes in the (7,6)-sample and (7,5)-sample.

	(n,m)	d_t (nm)	α (deg)	$E_{11} \pm 0.001$ (eV)	$E_{22} \pm 0.009$ (eV)
(7,5)-sample	(7,5)	0.829	24.50	1.205	1.916
(7,6)-sample	(7,6)	0.895	27.46	1.101	1.914
	(7,5)	0.829	24.50	1.209	1.925
	(8,3)	0.782	15.30	1.297	1.862

In both configurations in order to obtain a high sensitivity of the setup, the lock-in technique combined with balance detection is applied. The modulation of the pump beam is performed by an acousto-optical modulator (AOM) at a frequency of about 127 kHz to suppress noise.

The standard experimental pump-probe curve is shown in Fig. 7 and is discussed in Sec. IV A. All pump-probe curves, observed in our experiments, show three-exponential behavior with the few picosecond, tens of ps, and hundreds of ps to nanoseconds decay components. In this paper we focus our research on the first and the second decay components. Therefore all the curves shown here are limited by first 50 to 100 picoseconds of the decay curves, the background of the negative part of the curves is subtracted and signal is normalized to one at zero delay time.

III. THEORY

To understand the experiments, we carried out microscopic calculations based on carbon nanotube (CNT) Bloch equations including electron-phonon scattering applied to the specific nanotubes investigated here [24–27]. For modeling the performed experiments, we extend our calculations to a four-band CNT model including the optical allowed E_{11} and E_{22} transitions. To describe the dynamics of optically excited electrons we include their coupling to optical and acoustic phonon modes explicitly taking into account inter- and intrasubband relaxation channels. The laser pump process enters via a semiclassical carrier-light coupling. Applying the Heisenberg equation of motion for the relevant experimental quantities, we derive coupled equations for the microscopic polarization $p_k = \langle a^+_{V_2k} a_{C_2k} \rangle$ and carrier occupations $\rho^\lambda_k = \langle a^+_{\lambda k} a_{\lambda k} \rangle$ with $\lambda = C_1, C_2$ denoting the two energetically lowest conduction subbands, see Fig. 3. Treating the electron-phonon scattering terms up to second order Born-Markov approximation [3,26] we obtain:

$$\dot{p}_k = -i\,\Delta\omega_k\, p_k + i\,\Omega_k^{V_2C_2}\left(1 - 2\rho_k^\lambda\right) - \dot{p}_k|_{\text{deph}} \tag{1}$$

$$\dot{\rho}_k^\lambda = 2\Im\left(\left[\Omega_k^{V_2C_2}\right]^* p_k\right) + \dot{\rho}_k^\lambda|_{sc} \tag{2}$$

with $\hbar\Delta\omega_k = \varepsilon_k^{C_2} - \varepsilon_k^{V_2}$ denoting the band gap energy corresponding to E_{22}, $\Omega_k^{V_2C_2} = i\,\frac{e_0}{m_e} M_k^{V_2C_2} A(t)$ the Rabi frequency, with $A(t)$ as the vector potential. The optical matrix element $M_k^{V_2C_2}$ is based on tight binding wave functions containing the selection rules and the strength for the optical E_{22} transition [28,29]. As a first approach on the relaxation problem, the phonon-assisted intra- and intersubband scattering is assumed to be dominated by electron/hole-phonon interaction $\dot{\rho}_k^\lambda|_{sc}$, $\dot{p}_k|_{\text{deph}}$, i.e., we assume that due to strong dielectric screening of the surrounding medium excitonic effects do not have a significant qualitative influence on the observed relaxation behavior [23,30].

The basic processes included in Eqs. (1) and (2) are illustrated in Fig. 3: (a) electrons are pumped by the external laser field through the resonant transition E_{22} into the C_2 subband, (b) intersubband scattering via transversal optical (TO) phonons into the lower lying subband C_1, and (c) intrasubband electron relaxation through longitudinal acoustic (LA) phonons towards the band edge of C_1 into an equilibrium situation.

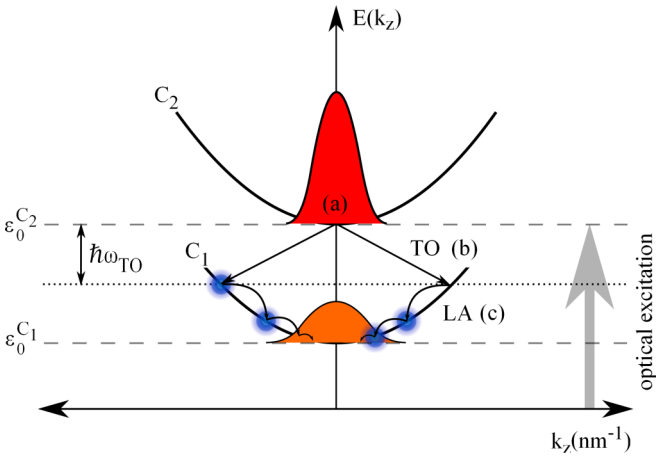

FIG. 3. (Color online) Sketch of the electron relaxation channels with TO and LA phonons around the K point for the (7,5) tube pumped at the E_{22} transition energy. The generated nonequilibrium electron occupation represented by the red Gaussian shaped distribution (a) scatters via intersubband emission of TO phonons into C_1 and relaxes intraband through interaction with LA phonons towards the band edge energy $\varepsilon_0^{C_1}$ into equilibrium, displayed by the Fermi distribution (orange).

We calculate the electron-phonon interaction terms as follows:

$$\dot{p}_k|_{\text{deph}} = \mathfrak{T}_k p_k + \mathfrak{U}_k \tag{3}$$

$$\dot{\rho}_k^{\lambda}|_{sc} = -\frac{2\pi}{\hbar}\sum_{q,\gamma,\pm}\sum_{\lambda'}^{C_1,C_2}\left|g_{k-q}^{\lambda\lambda'\gamma}\right|^2\delta\left(\varepsilon_{k'}^{\lambda'} - \varepsilon_k^{\lambda} \mp \hbar\omega_q^{\gamma}\right)F_{kk'q}^{\lambda\lambda'\gamma\pm}, \tag{4}$$

where the phonon induced dephasing of the polarization splits up into a diagonal

$$\mathfrak{T}_k = \frac{\pi}{\hbar}\sum_{q,\gamma,\pm}\sum_{\lambda\lambda'}^{C_2V_2}\left|g_{k-q}^{\lambda\lambda\gamma}\right|^2\delta\left(\varepsilon_{k'}^{\lambda'} - \varepsilon_k^{\lambda} \mp \hbar\omega_q^{\gamma}\right)X_{k'q}^{\lambda'\gamma\pm}$$

and an off-diagonal term

$$\mathfrak{U}_k = \frac{\pi}{\hbar}\sum_{q,\gamma,\pm}\sum_{\lambda\lambda'}^{V_2C_2}\left|g_{k-q}^{\lambda\lambda'\gamma}\right|^2\delta\left(\varepsilon_{k'}^{\lambda} - \varepsilon_k^{\lambda} \mp \hbar\omega_q^{\gamma}\right)Y_{kq}^{\lambda\gamma\pm}p_{k'}$$

with Pauli blocking and phonon emission and absorption contributions:

$$X_{k'q}^{\lambda'\gamma\pm} = \tilde{n}_{q\pm}^{\gamma}\rho_{k'}^{\lambda'} + \tilde{n}_{q\mp}^{\gamma}\left(1-\rho_{k'}^{\lambda'}\right),\quad Y_{kq}^{\lambda\gamma\pm} = \tilde{n}_{q\pm}^{\gamma}\left(1-\rho_k^{\lambda}\right) + \tilde{n}_{q\mp}^{\gamma}\rho_k^{\lambda}$$

and

$$F_{kk'q}^{\lambda\lambda'\gamma\pm} = \tilde{n}_{q\pm}^{\gamma}\rho_k^{\lambda}\left(1-\rho_{k'}^{\lambda'}\right) - \tilde{n}_{q\mp}^{\gamma}\rho_{k'}^{\lambda'}\left(1-\rho_k^{\lambda}\right)$$

with $\tilde{n}_{q\pm}^{\gamma} = n_q^{\gamma} + \frac{1}{2} \pm \frac{1}{2}$ and $k' = k \pm q$. Details on the matrix elements and further analytical treatment can be found in Ref. [26].

For the explicit evaluation of Eq. (4) optical and acoustic phonon modes at the K point are considered. Other CNT specific phonon modes like the radial breathing and twisting mode have less impact through their much weaker electron-phonon coupling elements [31]. Following the derivation of the electron-phonon coupling (EPC) elements for graphene

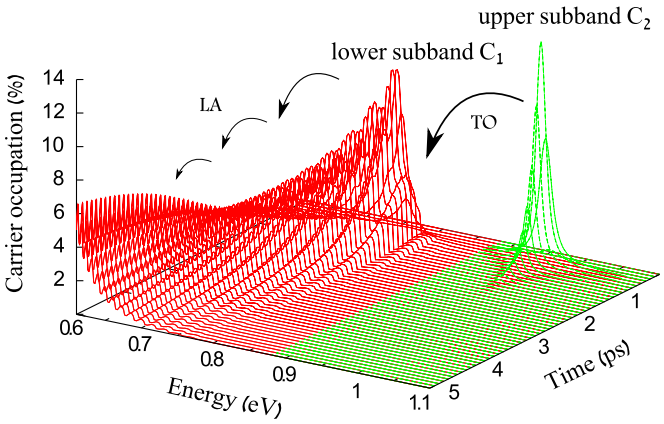

FIG. 4. (Color online) Time- and momentum-resolved inter- and intrasubband relaxation dynamics for the (7,5) tube. Carriers are excited to the band edge $\varepsilon_0^{C_2} = E_{22}/2$ via an optical pulse with a width of 190 fs. These scatter into C_1 under emission of optical (ΓTO) phonons within a few hundred femtoseconds and become redistributed via acoustic (ΓLA) phonons into a Fermi- like equilibrium on a picosecond timescale.

in the work of Piscanec *et al.* [32,33], it turns out that for CNTs intraband scattering is only possible with ΓTO phonons. We assume this to be valid also for interband scattering within the conduction subbands. The EPC for ΓTO phonons $|g_{CNT}^{\Gamma TO}|^2 = \frac{\sqrt{3}a_0^2}{\pi L}|g_{\text{graph}}^{\Gamma TO}|^2\frac{1}{d}$ shows the inverse dependence on the tube diameter d. Here, the lattice constant is $a_0 = 0.246$ nm, the EPC at the Γ point of graphene is $|g_{\text{graph}}^{\Gamma TO}|^2 = 0.0405\,\text{eV}^2$, and L is the length of the tube. The optical branch of the phonon dispersion around the Γ point is approximately constant $\hbar\omega_{q_0}^{\Gamma TO} \approx \epsilon_{q_0}^{\Gamma TO} = 192$ meV [34], and the optical phonon occupation $n_{q_0}^{\Gamma TO}$ is assumed to be a Bose-Einstein distribution at room temperature. The linear phonon dispersion for the acoustic mode in the vicinity of the Γ point is approximated by $\hbar\omega_q^{\Gamma LA} = \hbar c_s|q| \approx \beta^{\Gamma LA}|q|$, where the slope $\beta^{\Gamma LA} = 0.013\,\text{eVnm}$ is determined by the speed of acoustic phonons $c_s = 2\times10^4\frac{m}{s}$. The intraband coupling with ΓLA phonons is adapted from graphene [35] and yields $|g_{CNT}^{\Gamma LA}(q)|^2 = \frac{\hbar^2}{L}\frac{D^2}{\pi m\beta^{\Gamma LA}}\frac{1}{d}|q|$ where $m = 7.6\times10^{-8}\frac{\text{g}}{\text{cm}^2}$ is the mass density of carbon and $D = 16\,\text{eV}$ the deformation potential. An explicit analysis shows that intersubband relaxation via ΓLA phonon-electron scattering does not occur, since the energy difference between the lowest lying conduction subbands at the K point cannot be bridged.

Now, we evaluate the equations of motion Eqs. (1)–(4) for the carrier occupations under the following assumptions: (i) Resonant optical pumping of the E_{22} transition with a pulse width of 190 fs generating a nonequilibrium distribution at the band edge of C_2. (ii) We monitor only the occupations in the conduction subbands C_1, C_2. The holes in the valence subbands show similar relaxation behavior due to their identical band curvature. (iii) For the phonon-induced dephasing of the microscopic polarization p_k we extract an average dephasing rate $\hbar\gamma = 12.5$ meV given approximately by contributions of the diagonal and off-diagonal electron-phonon scattering rates, see Eq. (3).

The calculated carrier occupations are depicted in Fig. 4 as a function of energy and time for the experimentally

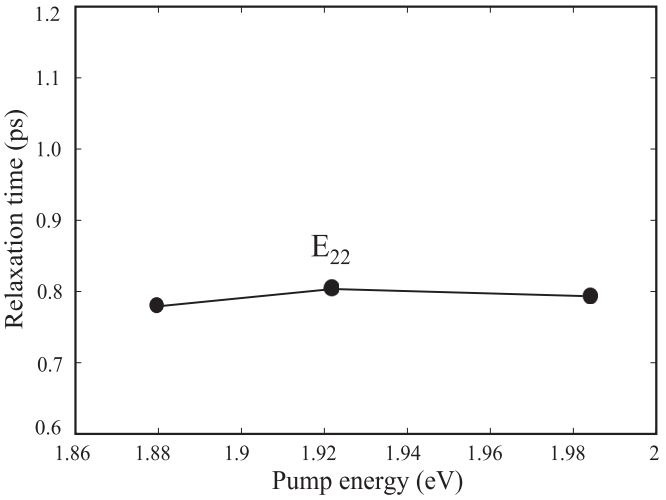

FIG. 5. Relaxation times vs pump energy at the constant probe energy of 1.3 eV for the (7,6) tube displaying that the dynamics remains nearly unaffected.

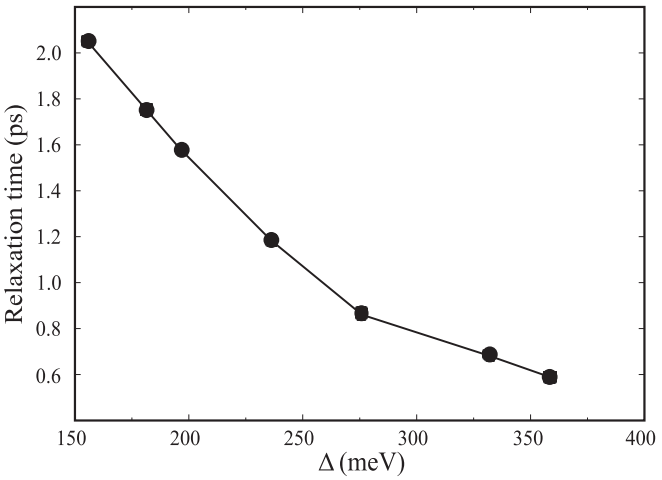

FIG. 6. Relaxation time vs probe energy at the constant pump energy of 1.92 eV corresponding to E_{22} transition for the (7,5) tube illustrating an acceleration of the dynamics towards higher energies (here $\Delta = E_{\text{probe}} - E_{11}^{(7,5)}$).

investigated (7,5) tube. Already during the action of the pulse, the distribution relaxes during the first hundred femtoseconds through intersubband scattering via optical phonons (ΓTO) into the lower subband C_1 generating the occupation peak at 0.77 eV after 1 ps and directly reflects the experimental rise time. For this, the dominant process is the emission of optical phonons with the energy $\epsilon_{q_0}^{\Gamma TO} = 192$ meV. The intraband scattering within the lowest subband C_1 via ΓLA phonons leads to a Fermi distribution on a picosecond timescale, cp. the thermal occupation after 5 ps in Fig. 4. The average relaxation times at certain probe energies can be obtained by exponential fits of the temporal decay of the electronic distribution.

A detailed analysis shows that the relaxation times only weakly depend on the pump energy, since the relaxation dynamics does not depend on the optically induced initial carrier occupation. Indeed, Fig. 5 shows that the change of the initial energetic position of the nonequilibrium carrier distribution determined by the pump energy has no significant impact on the following redistribution process in the C_1 band driven with ΓTO phonons by the fast intersubband scattering. On the other hand, Fig. 6 shows that varying the probe photon energies at fixed pump energy significantly changes the relaxation dynamics. When probing at higher energies in the subband C_1, cp. Fig. 3, the phonon momentum transfer q for an allowed scattering process via acoustic phonons is increased. Therefore, the linear q dependence of the acoustic EPC $|g_{CNT}^{\Gamma LA}(q)|^2 \propto |q|$ results in stronger coupling, and the decay of the carrier population is accelerated leading to decreasing relaxation times, as observed in Fig. 6. Thus, the observed acceleration of the temporal decay can be viewed as an indication of intraband scattering with acoustic phonons.

IV. RESULTS AND DISCUSSION

A. Decay curves under resonant to the tubes transition energies pumping and probing

In this subsection we present the results of the resonant pump-probe measurements, where the excitation is tuned resonant to E_{22} transition energy and probing is resonant to the E_{11} transition energy of the certain tube species. Figure 7 presents a differential transmission (DT) signal for both sets of samples: (7,5)-sample pumped at E_{22} and probed at E_{11} transitions of (7,5) tubes (black curve) and (7,6)-sample pumped at E_{22} and probed at E_{11} of (7,6) and (7,5) tubes accordingly (red and green curves). For these experiments the pump energy for all three curves was tuned to 1.924 eV (±2 meV), with FWHM 8 meV. The probe energies for the black and green curve were 1.209 eV (±1 meV), with FWHM 8 meV, and for the red curve 1.102 eV (±2 meV), with FWHM 10 meV. Since the luminescence and absorption peaks are quite broad (see Figs. 1 and 2), we assume these conditions to correspond to the resonant pump-probe measurements for each DT curve.

In the inset the three-exponential fitting curve of the differential transition signal of the (7,5) tubes [in (7,5)-sample] is shown. As for all pump-probe curves, which will be shown in the following sections, in Fig. 7 the differential transmission pump-probe signal is shown at the vertical logarithmic scaled axis, and the time delay between pump and probe pulses at the horizontal axis.

The black and red curves in Fig. 7 (corresponding to resonant pump-probe curves of (7,5) tubes in (7,5)-sample and (7,6) tubes in (7,6)-sample, respectively) show similar, if not identical, relaxation dynamics. Such behavior is expected, since (7,5) and (7,6) tubes have similar chirality angles, very close radii, as well as transition energies (see Table I), thus we believe their decay dynamics should be quite similar as well [26]. The green curve in Fig. 7, corresponding to resonant pump-probe curves of (7,5) tubes in (7,6)-sample, exhibit slightly faster initial decay dynamics than the other presented curves. Although the acceleration is fairly small, it is obvious and can be caused by the intermixing of two signals: the signal (i) stemming from (7,5) tube and (ii) from the (7,6) tube, probed at the energy equal to the transition energy E_{11} of the (7,5) tube ($E_{11}^{(7,5)}$), which is higher by about 100 meV than the E_{11} transition energy of the (7,6) tube ($E_{11}^{(7,6)}$). In support

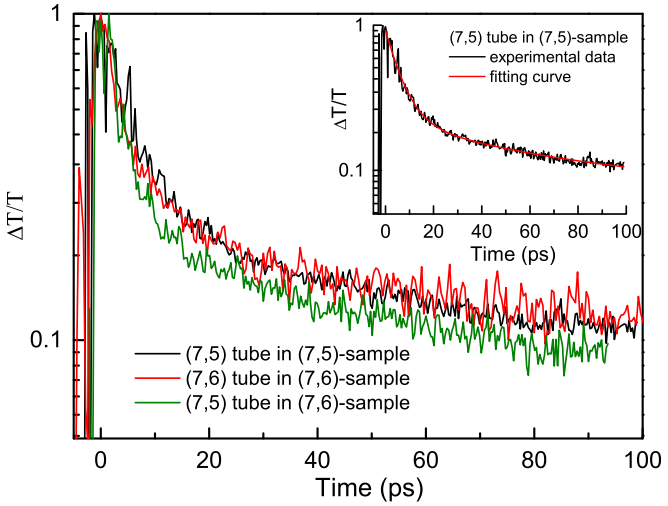

FIG. 7. (Color online) Differential transmission signal as a function of the delay time between pump and probe pulses. Energies of the probe and pump pulses are tuned resonant to E_{11} and E_{22} transition energies (respectively) of the (7,5) species in both (7,5)- and (7,6)-samples (black and green curves, respectively) and of the (7,6) species in the (7,6)-sample (red curve). On the inset an example of the tree-exponential fit of the experimental curve is presented.

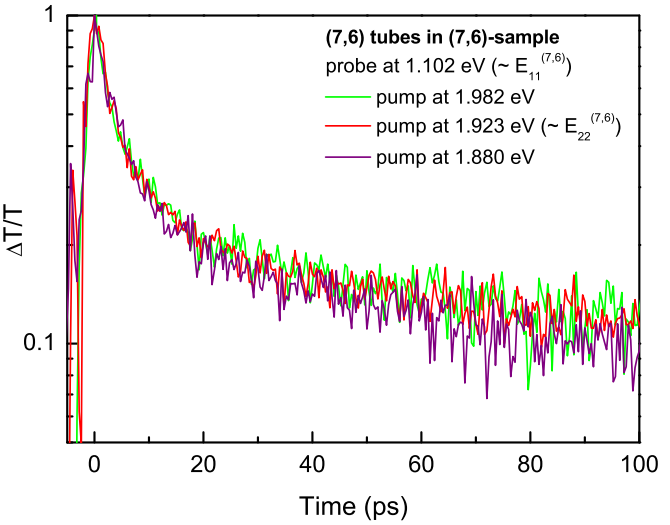

FIG. 8. (Color online) Differential transmission signal as a function of the delay time between pump and probe pulses measured for (7,6)-sample. Energy of the probe pulse is fixed to the 1.102 eV, close to the $E_{11}^{(7,6)}$ energy. Energy of the pump pulse is tuned to 1.982, 1.923 (close to $E_{22}^{(7,6)}$) and 1.880 eV (green, red and purple color respectively).

of this presumption, our calculations (see Chap. III) as well as our experimental results (see Chap. IV C) evidence, that the SW-CNTs carrier relaxation is accelerated when probed at the higher energies. However, such processes as energy transfer between tubes could also result in a similar effect. More research is required in order to distinguish between these effects.

B. Pump energy tuning

In order to exclude potential influence of the pump energy on the observed relaxation dynamics we perform pump-probe experiments with fixed probe energy and three different pump energies. The probe energy is equal to 1.102 eV ($\simeq E_{11}^{(7,6)}$, within an error bar), and pump energy being tuned to 1.982, 1.923 ($\simeq E_{22}^{(7,6)}$, within an error bar) and 1.880 eV (see green, red, and purple curves in Fig. 8, respectively).

In spite of relatively large energy tuning range ($\pm$50 meV), we observe no appreciable changes in the differential transmission signal for different pump energies. Theoretical calculations support our experimental results for the first picosecond decay component, which shows no significant difference depending on the pump energy, revealing that the energy point where the pumped nonequilibrium electrons enter has no influence on the further decay strength of the carrier population (see Chap. III for more details). Indeed the τ_1 calculated for the pump energies detuned from the E_{22} resonance of the (7,6) tube for the same values as in experiment exhibit no significant variations (see Fig. 5).

C. Probe energy tuning

In this subsection we present our investigation of the relaxation dynamics dependency on the probe energy. The measurements were conducted on the (7,5)-sample, pumping at the 1.924 eV ($\simeq E_{22}^{(7,5)}$), and probing at four different energies: 1.209 ($\simeq E_{11}^{(7,5)}$), 1.244, 1.481, and 1.563 eV. In Fig. 9 two differential transmission signals for the lowest and the highest probe energies (black and blue curve, respectively) are shown. In accordance with theoretical calculations we observe an acceleration in the differential transmission signal with tuning the probe energies toward the higher values, denoted with arrow in Fig. 9.

In Table II the first two components of the decay dynamics (τ_1^{exp} and τ_2^{exp}) for four probing energies (E_{probe}) are shown. The broadness of the probing pulses (FWHM) as well as the

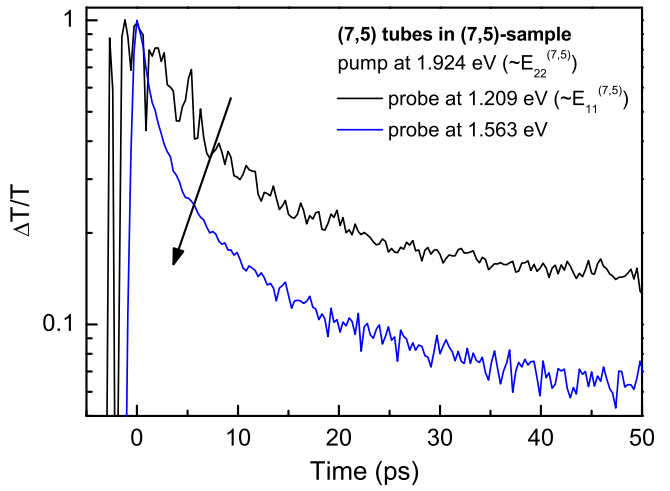

FIG. 9. (Color online) Differential transmission signal as a function of the delay time between pump and probe pulses measured for (7,5)-sample. Energy of the pump pulse is fixed to the 1.924 eV, close to the $E_{22}^{(7,5)}$ energy. Energy of the probe pulse is equal to 1.209 (close to $E_{11}^{(7,5)}$) and 1.563 eV (black and blue curves, respectively).

TABLE II. List of the determined relaxation times for the (7,5)-sample, pumped at 1.924 eV and probed at four different energies, listed in the table. The difference between the probe energy and transition energy E_{11} is denoted by Δ ($= E_{\text{probe}} - E_{11}^{(7,5)}$). Theoretically calculated decay times are shown for comparison.

E_{probe} (eV)	FWHM (meV)	Δ (meV)	τ_1^{exp} (ps)	τ_2^{exp} (ps)	Δ (meV)	τ_1^{theo} (ps)
1.209	8	4	5.8 ± 0.4	50 ± 10	156	2.04
1.244	9	38	4.5 ± 0.4	23 ± 6	180	1.76
1.481	18	276	2.0 ± 0.2	8 ± 2	276	0.86
1.563	19	358	1.6 ± 0.1	10 ± 1	358	0.59

offset of the probe energy according to the (7,5) tubes E_{11} transition energy (Δ) are shown in Table II as well.

The first decay component exhibits similar values and equivalent dependency on the Δ as theoretically calculated relaxation times (τ^{theor}) which are related to stronger acoustic phonon coupling for probing at higher energy points in the band structure. Thus we present the evidence that the few picosecond dynamics observed in our experimental studies is caused by the scattering of the carriers with acoustic phonons. In addition, for chirality-enriched samples the experimentally observed τ_1^{exp} is quantitatively better described by theoretically calculated relaxation dynamics, if compared to the ensemble samples (see Ref. [16]). However, the focus of our theoretical study lies on a qualitative understanding of the elementary scattering processes and our calculations, based on microscopic Bloch equations, do not include adjustable parameters. The quantitative deviations of the predicted scattering times with the experimentally observed ones can probably be traced back to neglected excitonic effects and the missing interaction with the surrounding medium.

The second and the third relaxation times also show acceleration for the higher energy probing. However, for the probing at 1.481 eV we observe higher acceleration of the τ_2^{exp}, as for the probing at 1.563 eV. We believe that the 1.481 eV energy could be in resonance to some triplet state since it hits about 300 meV above the E_{11} transition energy (see Ref. [36]) and therefore could exhibit a singularity in the behavior.

V. SUMMARY

We have studied the relaxation dynamics in chirality-enriched SW-CNTs by two-color pump-probe. We demonstrate the acceleration of relaxation dynamics for probing at higher energies from the E_{11} transition while keeping the pump energy fixed to E_{22} transition energy. We also found that the dynamics is independent on the pump energy while probe energy is kept constant. The results fit well to the presented theoretical investigations revealing that acoustic phonons have the main impact to the observed relaxation times in the range of a few picoseconds while optical phonons enable intersubband scattering.

ACKNOWLEDGMENTS

Rishabh M. Jain gratefully acknowledges support from the National Science Foundation Graduate Research Fellowship and the Department of Defense through the National Defense Science and Engineering Graduate Fellowship.

[1] G. D. Ado Jorio and M. S. Dresselhaus, *Carbon nanotubes: advanced topics in the synthesis, structure, properties and applications* (Springer, Berlin, 2008).
[2] C. T. Stephanie Reich and J. Maultzsch, *Carbon Nanotubes: Basic Concepts and Physical Properties* (Wiley-VCH, Berlin, 2004).
[3] E. Malic and A. Knorr, *Graphene and Carbon Nanotubes: Ultrafast Relaxation Dynamics and Optics* (Wiley-VCH, Berlin, 2013).
[4] N. Behabtu, C. C. Young, D. E. Tsentalovich, O. Kleinerman, X. Wang, A. W. K. Ma, E. A. Bengio, R. F. ter Waarbeek, J. J. de Jong, R. E. Hoogerwerf, S. B. Fairchild, J. B. Ferguson, B. Maruyama, J. Kono, Y. Talmon, Y. Cohen, M. J. Otto, and M. Pasquali, Science **339**, 182 (2013).
[5] A. Cao, P. L. Dickrell, W. G. Sawyer, M. N. Ghasemi-Nejhad, and P. M. Ajayan, Science **310**, 1307 (2005).
[6] D. J. Lipomi, M. Vosgueritchian, B. C.-K. Tee, S. L. Hellstrom, J. A. Lee, C. H. Fox, and Z. Bao, Nat. Nanotechnol. **6**, 788 (2011).
[7] W. Yang, K. R. Ratinac, S. P. Ringer, P. Thordarson, J. J. Gooding, and F. Braet, Angew. Chem., Int. Ed. **49**, 2114 (2010).
[8] M. Endo, M. Strano, and P. Ajayan, in *Carbon Nanotubes*, Topics in Applied Physics Vol. 111, edited by A. Jorio, G. Dresselhaus, and M. Dresselhaus (Springer, Berlin, Heidelberg, 2008), pp. 13–62.
[9] C. Manzoni, A. Gambetta, E. Menna, M. Meneghetti, G. Lanzani, and G. Cerullo, Phys. Rev. Lett. **94**, 207401 (2005).
[10] G. Lanzani, G. Cerullo, A. Gambetta, C. Manzoni, E. Menna, and M. Meneghetti, Synth. Met. **155**, 246 (2005).
[11] J. Park, P. Deria, and M. J. Therien, J. Am. Chem. Soc. **133**, 17156 (2011).
[12] M. W. Graham, J. Chmeliov, Y.-Z. Ma, H. Shinohara, A. A. Green, M. C. Hersam, L. Valkunas, and G. R. Fleming, J. Phys. Chem. B **115**, 5201 (2011).
[13] G. N. Ostojic, S. Zaric, J. Kono, M. S. Strano, V. C. Moore, R. H. Hauge, and R. E. Smalley, Phys. Rev. Lett. **92**, 117402 (2004).
[14] I. Rubtsov, R. Russo, T. Albers, P. Deria, D. Luzzi, and M. Therien, Appl. Phys. A: Mater. Sci. Process. **79**, 1747 (2004).
[15] J.-P. Yang, M. M. Kappes, H. Hippler, and A.-N. Unterreiner, Phys. Chem. Chem. Phys. **7**, 512 (2005).
[16] O. A. Dyatlova, C. Khler, E. Malic, J. Gomis-Bresco, J. Maultzsch, A. Tsagan-Mandzhiev, T. Watermann, A. Knorr, and U. Woggon, Nano Lett. **12**, 2249 (2012).
[17] B. Gao, G. V. Hartland, and L. Huang, J. Phys. Chem. Lett. **4**, 3050 (2013).
[18] Y. Ohno, S. Iwasaki, Y. Murakami, S. Kishimoto, S. Maruyama, and T. Mizutani, Phys. Status Solidi B **244**, 4002 (2007).

[19] K. Tvrdy, R. M. Jain, R. Han, A. J. Hilmer, T. P. McNicholas, and M. S. Strano, ACS Nano **7**, 1779 (2013).
[20] R. M. Jain, K. Tvrdy, R. Han, Z. Ulissi, and M. S. Strano, ACS Nano **8**, 3367 (2014).
[21] H. Liu, D. Nishide, T. Tanaka, and H. Kataura, Nat. Commun. **2**, 309 (2011).
[22] S. M. Bachilo, M. S. Strano, C. Kittrell, R. H. Hauge, R. E. Smalley, and R. B. Weisman, Science **298**, 2361 (2002).
[23] O. A. Dyatlova, J. Gomis-Bresco, E. Malic, H. Telg, J. Maultzsch, G. Zhong, J. Geng, and U. Woggon, Phys. Rev. B **85**, 245449 (2012).
[24] M. Hirtschulz, F. Milde, E. Malić, S. Butscher, C. Thomsen, S. Reich, and A. Knorr, Phys. Rev. B **77**, 035403 (2008).
[25] C. Köhler, T. Watermann, and E. Malic, Phys. Status Solidi B **249**, 2483 (2012).
[26] C. Köhler, T. Watermann, and E. Malic, J. Phys.: Condens. Matter **25**, 105301 (2013).
[27] E. Malic, J. Maultzsch, S. Reich, and A. Knorr, Phys. Rev. B **82**, 035433 (2010).
[28] A. Grüneis, R. Saito, G. G. Samsonidze, T. Kimura, M. A. Pimenta, A. Jorio, A. G. Souza Filho, G. Dresselhaus, and M. S. Dresselhaus, Phys. Rev. B **67**, 165402 (2003).
[29] E. Malic, M. Hirtschulz, F. Milde, A. Knorr, and S. Reich, Phys. Rev. B **74**, 195431 (2006).
[30] E. Malic, M. Hirtschulz, J. Maultzsch, S. Reich, and A. Knorr, Phys. Status Solidi B **246**, 2592 (2009).
[31] M. Machón, S. Reich, H. Telg, J. Maultzsch, P. Ordejón, and C. Thomsen, Phys. Rev. B **71**, 035416 (2005).
[32] S. Piscanec, M. Lazzeri, J. Robertson, A. C. Ferrari, and F. Mauri, Phys. Rev. B **75**, 035427 (2007).
[33] S. Piscanec, M. Lazzeri, F. Mauri, A. C. Ferrari, and J. Robertson, Phys. Rev. Lett. **93**, 185503 (2004).
[34] J. Maultzsch, S. Reich, C. Thomsen, H. Requardt, and P. Ordejón, Phys. Rev. Lett. **92**, 075501 (2004).
[35] W.-K. Tse and S. Das Sarma, Phys. Rev. B **79**, 235406 (2009).
[36] S. Tretiak, Nano Lett. **7**, 2201 (2007).